Nano Research

Open Access

Research Article

# A green-solvent strategy for uniform perovskite thick films in X-ray detection

Shuan Kuang[1,§], Ziqiang Chen[1,3,§], Guanlin Huang[1], Mingquan Liao[1], Guangya Zheng[1], Yinsheng Xu[2], Tongle Bu[3], Guoqiang Luo[1,4,5], Xin He[6] ✉, Guangda Niu[7] ✉, and Mengling Xia[1] ✉

[1] *School of Materials Science and Engineering, Wuhan University of Technology, Wuhan 430070, China*
[2] *State Key Laboratory of Silicate Materials for Architectures, Wuhan University of Technology, Wuhan 430070, China*
[3] *State Key Laboratory of Advanced Technology for Materials Synthesis and Processing, Wuhan University of Technology, Wuhan 430070, China*
[4] *Chaozhou Branch of Chemistry and Chemical Engineering Guangdong Laboratory, Chaozhou 521000, China*
[5] *Hubei Technology Innovation Center for Advanced Composites, Wuhan University of Technology, Wuhan 430070, China*
[6] *Key Laboratory of Flexible Optoelectronic Materials and Technology, Ministry of Education, Jianghan University, Wuhan 430056, China*
[7] *Wuhan National Laboratory for Optoelectronics, Huazhong University of Science and Technology, Wuhan 430074, China*
[§] *Shuan Kuang and Ziqiang Chen contributed equally to this work.*

**Cite this article:** *Nano Research*, **2026**, *19*, 94908380. https://doi.org/10.26599/NR.2026.94908380

**ABSTRACT:** Perovskite polycrystalline films have gained considerable attention as promising materials for X-ray imaging applications. However, the conventional fabrication of perovskite-based X-ray detectors typically relies on large quantities of highly toxic solvents, especially since the absorber layer must reach thicknesses of hundreds of micrometers to ensure sufficient X-ray attenuation. To address this issue, we employed green and non-toxic γ-valerolactone (GVL) as the solvent for fabricating $MAPbI_3$ perovskite thick films. Accompanying this, an ultrasonic-assisted annealing process was introduced to mitigate the irregular migration and inhomogeneous distribution of solute ions resulting from the weak coordination between GVL and $Pb^{2+}$. This combined strategy enabled the production of $MAPbI_3$ thick films with remarkable uniformity in both horizontal and vertical directions. The inhomogeneity values below 38.19% along the vertical axis and less than 6.6% in the horizontal plane were achieved, exhibiting an 84% improvement in dark current uniformity over films prepared by conventional annealing methods. Furthermore, the resulting $MAPbI_3$ thick-film detector exhibits a high X-ray detection sensitivity and a high imaging resolution of 4.46 lp·mm$^{-1}$. This work provides a robust and eco-friendly approach to the fabrication of high-performance and stable perovskite thick films for advanced radiation detectors.

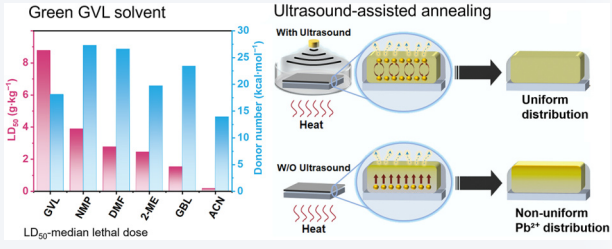


**KEYWORDS:** green solvent, perovskite polycrystalline films, ultrasonic-assisted annealing, uniformity, X-ray detection

## 1 Introduction

X-ray detectors are crucial in various fields, including medical imaging, security inspection, and scientific research [1]. Recently, halide perovskite materials have emerged as promising candidates for next-generation high-energy radiation detectors, owing to their high atomic number, large carrier mobility-lifetime product ($\mu\tau$), and low trap density ($10^7$–$10^9$ cm$^{-3}$), etc. [2–5]. In particular, perovskite polycrystalline films, which can be easily synthesized on a large scale and deposited onto commercially available substrates, have demonstrated great potential for practical X-ray imaging applications [6–8]. However, the fabrication of perovskite polycrystalline X-ray detectors often involves the use of highly toxic solvents, such as N,N-dimethylformamide (DMF), dimethyl sulfoxide (DMSO), and γ-butyrolactone (GBL). Moreover, to ensure complete X-ray absorption, perovskite thick films generally need to reach thicknesses on the order of hundreds of micrometers [9, 10]. While in perovskite photovoltaics, 1 mL of precursor solution can be used to fabricate up to ten films, each covering several square centimeters, the same volume can produce only one film of similar size for X-ray detectors. This leads to a significant increase in solvent consumption, posing potential hazards to

**Received:** December 14, 2025
**Accepted:** December 26, 2025

✉Address correspondence to Xin He, hexin@jhun.edu.cn; Guangda Niu, guangda_niu@hust.edu.cn; Mengling Xia, xiamengling@whut.edu.cn

human health and the environment, and contradicting the global carbon-neutrality strategy. Therefore, there is an urgent need to develop green solvent systems for the fabrication of perovskite polycrystalline X-ray detectors [11].

Inspired by advances in photovoltaics and chemical engineering, we identified γ-valerolactone (GVL) as a promising green and non-toxic alternative to GBL for preparing $MAPbI_3$ precursor solutions and thick films [12, 13]. GVL is typically synthesized via the hydrogenation of levulinic acid, a hydrolyzate of lignocellulose, and can sometimes be directly applied as a food additive [14, 15]. Moreover, GVL's metabolic byproducts *in vivo* are non-toxic, with valeric acid as the primary product, and the five-membered ring structure of GVL offers greater stability and is hard to degrade into harmful substances [15]. Toxicity evaluations confirm that GVL is five times less toxic than GBL (Table S1 in the Electronic Supplementary Material (ESM)). However, the lower complexation constant (Kf) of GVL with $Pb^{2+}$ reduces the solubility of $MAPbI_3$ compared to that in GBL, resulting in a more viscous solution to achieve the same degree of supersaturation [16, 17]. In the solvent evaporation process, due to the poor affinity between GVL and $Pb^{2+}$, the decreased decoordination energy barrier of the iodoplumbate/solvent complexes leads to $Pb^{2+}$ migration along with the solvent to the surface and leads to vertical inhomogeneity [18, 19]. The elevated viscosity further exacerbates uneven solute distribution during annealing, detrimentally affecting film performance [20]. Therefore, achieving uniform and high-performance perovskite thick films using the green solvent GVL remains a substantial challenge.

Herein, we proposed an ultrasonic-assisted annealing process to inhibit the irregular migration and uneven distribution of solute ions using green GVL solvent. Our method produces $MAPbI_3$ perovskite thick films with exceptional morphological smoothness and compositional homogeneity in both horizontal and vertical directions. Quantitative analysis of the $Pb^{2+}$ distribution uniformity along the longitudinal direction within a 45 μm depth range showed a 21.5% improvement in homogeneity for ultrasound-assisted annealed perovskite thick films, as indicated by a reduced coefficient of variation (CV, calculated as (standard deviation/mean) × 100%). Simultaneously, in the transverse direction, the dark current non-uniformity was significantly reduced to a CV of 6.6% following ultrasound-assisted annealing, far below the 41.43% observed in conventionally processed films. Additionally, the $MAPbI_3$ perovskite thick film detector shows a high X-ray detection sensitivity and imaging resolution (4.46 $lp \cdot mm^{-1}$). This work presents a novel approach to fabricating high-performance, environmentally friendly, and stable perovskite thick films for advanced radiation detectors.

## 2 Results and discussion

Stable perovskite inks are essential for fabricating high-quality thick films. The solubility curves of $MAPbI_3$ in GVL and GBL solvents are shown in Fig. S1 in the ESM. To evaluate the stability of perovskite precursors in different solvents, supersaturated solutions (4.5 M) were prepared by dissolving stoichiometric mixtures of methylammonium iodide (MAI) and $PbI_2$ in GVL and GBL, respectively, with their molecular structures illustrated in Fig. 1(a) (experimental details provided in the ESM). After static standing for 12 h at room temperature, the GBL-based precursor solution showed significant phase separation, whereas the GVL-based solution remained a homogeneous and stable black slurry (Fig. S2 in the ESM). This difference can be attributed to the Gutmann donor number (DN), which quantifies the solvent's Lewis basicity and its coordination ability with $Pb^{2+}$. A higher DN value, as for GBL, indicates stronger coordination, leading to more stable iodoplumbate complexes in the precursor solution. In contrast, the lower DN of GVL results in weaker coordination and less stable complexes, which compromise the kinetic control over crystallization during annealing. The median lethal dose ($LD_{50}$) and DN values of different solvents commonly employed in perovskite fabrication are summarized in Fig. 1(b). The DN values for GVL and GBL are 18.1 and 23.4, respectively, consistent with the observed stability behavior of the two solutions. Also, compared with other environmentally friendly solvents such as dimethyl carbonate and 2-methoxyethanol, GVL offers superior overall performance of high boiling point, viscosity suitable for blade coatings, validated low toxicity, and sufficient solubility for perovskites.

The $MAPbI_3$@GVL precursor solution was blade-coated onto an fluorine-doped tin oxide (FTO) glass substrate and immediately subjected to ultrasonic-assisted annealing (named as UA-annealing) in a 60 °C bath for 1 h. This step was followed by a multi-stage thermal annealing process at 60 °C (2 h), 80 °C (2 h), and 100 °C (3 h). For comparison, a control sample was prepared using conventional thermal annealing (named as C-annealing) without ultrasound assistance for over 8 h. UA-annealing yielded a significantly smoother perovskite thick film relative to C-annealing (Fig. S3 in the ESM). This improvement is attributed to ultrasonic cavitation, which reduces surface tension and enhances surface leveling during solvent evaporation [21, 22]. More importantly, ultrasound irradiation promoted uniform film formation and suppressed inhomogeneous ion migration caused by concentration gradient-driven solvent diffusion (Fig. 1(c)).

In an ultrasonic field, the high-frequency oscillation of liquid molecules—combined with the relatively high viscosity of the liquid medium—enables significant energy absorption from the propagating acoustic wave. The resulting high acoustic pressure disrupts intermolecular interactions within the solvent, generating numerous cavitation bubbles. The asymmetric collapse of these bubbles near solid interfaces (such as the substrate or $MAPbI_3$ particles) produces high-speed microjets that impinge on the surface. This microjet impact is the primary mechanism responsible for localized mechanical effects, including the fragmentation of brittle particulates and surface erosion. The transient peak pressure ($P_{jet}$) generated during microjet impact can be semi-quantitatively estimated using the water hammer pressure equation [23]

$$P_{jet} = \rho c V_{jet} \quad (1)$$

where $\rho$ is the density of the solution, $c$ denotes the speed of sound in the solution, and $V_{jet}$ signifies the jet impact velocity. Taking $\rho$ = 1100 $kg \cdot m^{-3}$, $c$ = 1400 $m \cdot s^{-1}$, and $V_{jet}$ = 114 $m \cdot s^{-1}$, a preliminary calculation estimates the transient peak pressure generated by the microjet to be approximately 0.175 GPa [24]. This immense, localized mechanical force is the key to overcoming a major bottleneck in green-solvent processing. Researchers have observed that in viscous, supersaturated precursor, unreacted $PbI_2$ is often encapsulated by a shell of initially formed $MAPbI_3$, which hinders its complete reaction with MAI during conventional annealing [25]. The calculated microjet impact pressure (~ 0.175 GPa) significantly surpasses the mechanical strength of the $MAPbI_3$ encapsulation (on

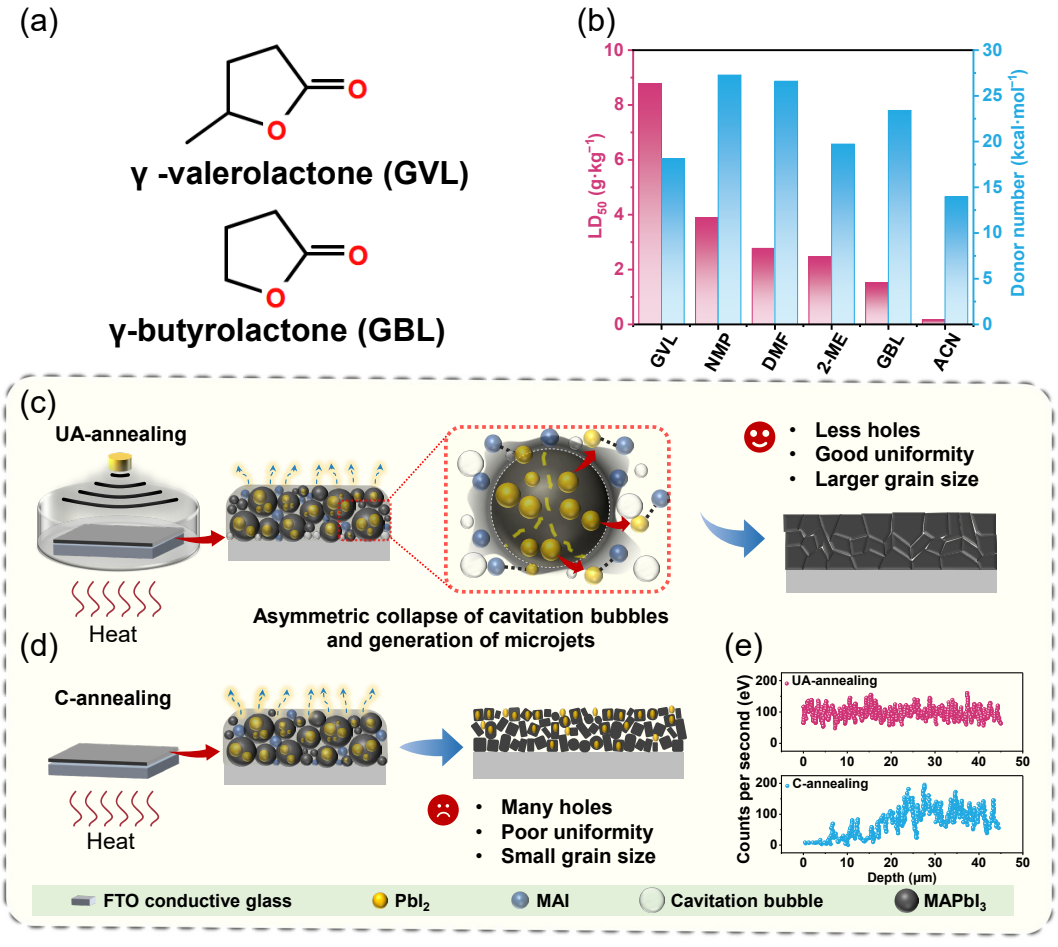


**Figure 1** (a) Structural formulas of GVL and GBL solvents. (b) Donor number values and median lethal dose ($LD_{50}$) of different solvents widely used in perovskite preparation. (c) and (d) Schematic diagrams of UA-annealing and C-annealing processes for $MAPbI_3$ thick films, along with the cavitation effect generated by ultrasound and the role of microjet. (e) Linear scanning EDS of $Pb^{2+}$ distribution in the vertical cross-section of $MAPbI_3$ thick films prepared by UA-annealing and C-annealing.

the order of ~ 10 MPa) [26]. Consequently, the microjet effectively fragments the encapsulating shell, liberating the confined $PbI_2$ particles. Subsequently, the released $PbI_2$, now with drastically increased surface area and dispersion, can readily and homogeneously react with the surrounding MAI. Furthermore, the intense micro-scale turbulence and streaming induced by cavitation provide unparalleled mixing, ensuring a uniform distribution of reactants. This synergistic process—where physical fragmentation via cavitation enables homogeneous chemical reaction—ensures a more stoichiometric and spatially consistent conversion to $MAPbI_3$ throughout the entire film thickness. Therefore, the UA annealing strategy directly addresses the root cause of vertical inhomogeneity in green-solvent-processed thick films by actively mitigating the irregular migration and aggregation of solute ions, leading to the observed superior compositional uniformity. As shown in Fig. 1(e), the thick film with UA-annealing shows a uniform $Pb^{2+}$ distribution without an obvious vertical concentration gradient from the substrate to the film surface. In contrast, the C-film exhibited a significant $Pb^{2+}$ gradient distribution, particularly the position below 20 μm from the substrate (0 μm), the X-ray diffraction (XRD) results also detected distinct characteristic peaks of $PbI_2$, due to the migration of solvent-ion complexes towards the film surface (Figs. 1(d) and 2(a) and Fig. S5 in the ESM). Quantitative analysis of the longitudinal $Pb^{2+}$ distribution over a 45 μm depth revealed inhomogeneity values of 38.19% for the UA-annealing film, which is significantly lower than the 48.658% obtained for the C-annealing film, as indicated by a reduced CV. The same phenomenon was also observed in other element distributions (Fig. S4 in the ESM), further demonstrating the positive effect of UA-annealing for uniform perovskite thick film.

XRD analysis confirmed that both UA-annealing and C-annealing $MAPbI_3$ thick films exhibit diffraction peaks consistent with the tetragonal perovskite structure. However, the C-annealed film, with its inferior homogeneity, showed additional characteristic peaks of $PbI_2$ (Fig. 2(a)). The smaller full-width at half maximum (FWHM) of the film with UA-annealing indicated improved crystallinity (Fig. S5 and Table S2 in the ESM). As shown in Figs. 2(b) and 2(c), the grains on the surface of the UA-annealing thick film are closely connected, and there are almost no holes, while the surface of the thick film prepared by the C-annealing process has cracks and many holes, which will seriously affect the uniformity and performance of the thick film. Compared to traditional annealing methods, UA-annealing significantly improves film quality in two main ways. On one hand, it ensures a more uniform distribution of components, minimizing defects caused by compositional segregation. On the other hand, the inherently uneven surface of the FTO conductive glass poses a challenge for conventional doctor-blade coating methods, as the surface tension of the precursor solution often leads to poor interfacial contact. This results in weak adhesion, causing the

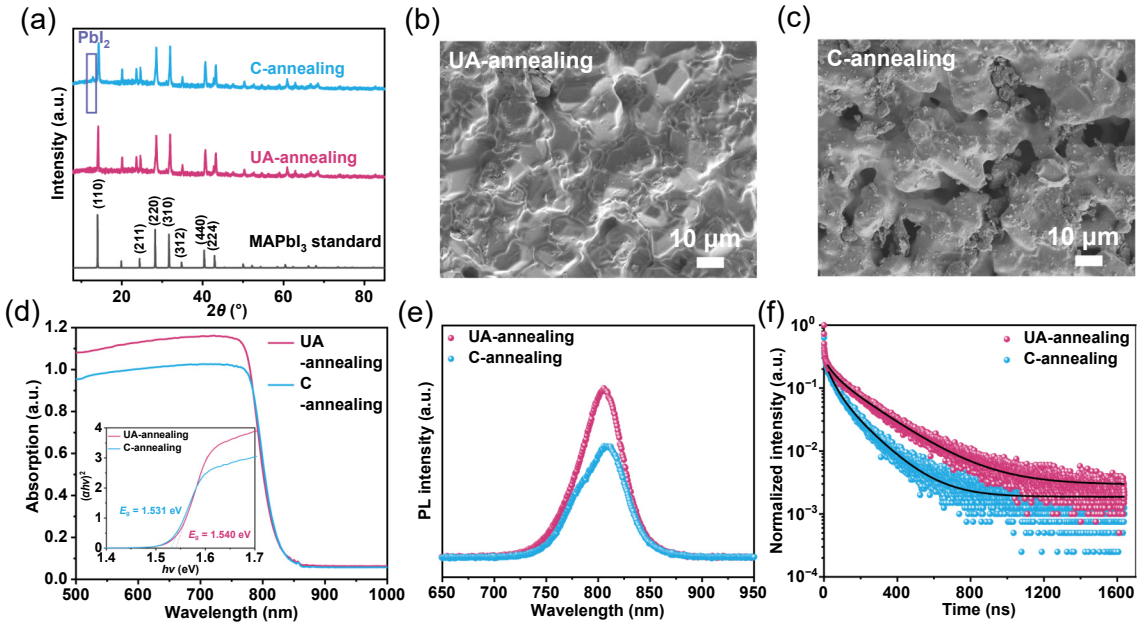


**Figure 2** (a) XRD patterns of $MAPbI_3$ thick films prepared via UA-annealing and C-annealing. SEM surface images of $MAPbI_3$ thick films prepared using (b) UA-annealing and (c) C-annealing. (d) Absorption spectra of $MAPbI_3$ thick films with or without UA-annealing. The inset is their bandgap diagram. (e) Steady-state PL spectra and (f) TRPL spectra of $MAPbI_3$ thick films with or without UA-annealing.

$MAPbI_3$ thick film to delaminate easily. In contrast, ultrasonic vibrations enhance the wetting of the precursor solution on the FTO substrate, enabling tighter grain packing and increased film density. This superior adhesion is demonstrated by the ability of the film to support an 850 g weight without detachment (Figs. S6 and S7 in the ESM). From the ultraviolet–visible (UV–vis) spectroscopy measured in a reflection mode, the direct bandgap of $MAPbI_3$ thick films can be derived through taut plot fitting, as shown in Fig. 2(d). The slight difference in the bandgap of $MAPbI_3$ thick films with and without UA-annealing may be attributed to surface compositional deviation. The uniform $MAPbI_3$ thick films exhibited a higher photoluminescence (PL) peak intensity and a narrower FWHM, further demonstrating the improved crystallinity of the thick film surface, as shown in Fig. 2(e). Finally, time-resolved photoluminescence (TRPL) spectroscopy was used to determine carrier lifetimes (Fig. 2(f) and Table S3 in the ESM), another important metric of film quality impacting device performance. The average carrier lifetime of the $MAPbI_3$ thick films prepared by UA-annealing was 202.87 ns, significantly longer than the 106.43 ns for those prepared by C-annealing, indicating reduced internal defects and suppressed non-radiative carrier recombination.

Uniform and dense films generally facilitate suppressed ion migration and non-radiative recombination of photoinduced carriers, thus improving carrier collection and X-ray detection performance. The temperature-dependent conductivity method previously established was utilized to quantify the activation energy for ion migration. At low temperatures, ion migration is effectively suppressed, and conductivity primarily results from electronic conduction. Conversely, at elevated temperatures, thermal activation of ionic conduction significantly enhances conductivity. The high-temperature region of the conductivity curves was fitted using the Nernst–Einstein equation [27]

$$\sigma(T) = \frac{\sigma_0}{T}\exp\left(-\frac{E_a}{K_B T}\right) \quad (2)$$

where $\sigma_0$ is a constant, $T$ is the temperature, $E_a$ is the activation energy for ion migration, and $k_B$ is the Boltzmann constant. As depicted in Fig. 3(a), the conductivity of $MAPbI_3$ films prepared via UA-annealing exhibited a transition at 200 K, compared to 160 K for C-annealing films. The activation energies for ion migration were 312.16 and 128.57 meV for UA-annealing and C-annealing films, respectively. These results confirm that UA-annealing inhibited ion migration within the $MAPbI_3$ thick films, reducing defects caused by non-uniform element distribution. Space-charge-limited current (SCLC) measurements quantified the electron and hole trap density ($n_{trap}$) using Eq. (3). The trap-filled limit voltage ($V_{TFL}$) was determined from the intersection point between the ohmic and trap-filled regions of the SCLC curves [28]

$$n_{trap} = \frac{2\varepsilon\varepsilon_0 V_{TFL}}{eL^2} \quad (3)$$

where $\varepsilon_0$ is the vacuum permittivity, e is the elementary charge, and $L$ is the film thickness. As shown in Fig. 3(b), the thick film with UA-annealing exhibited lower trap densities ($7.09 \times 10^{10}$ $cm^{-3}$) than the C-annealing film ($4.45 \times 10^{11}$ $cm^{-3}$), consistent with PL and PL decay results. The carrier mobility-lifetime product ($\mu\tau$), a critical parameter for carrier transport, was calculated using the modified Hecht equation (Fig. 3(c)) [10, 29]

$$I = \frac{I_0\mu\tau V}{L^2}\frac{\left(1-\exp\left(-\frac{L^2}{\mu\tau V}\right)\right)}{1+\frac{Ls}{V\mu}} \quad (4)$$

where $I_0$ is the saturation photocurrent, $V$ is the applied bias voltage, and $L$ is the film thickness. The $\mu\tau$ value of $MAPbI_3$ thick film with UA-annealing ($1.21 \times 10^{-3}$ $cm^2 \cdot V^{-1}$) is an order of magnitude higher than the C-annealing one ($1.05 \times 10^{-4}$ $cm^2 \cdot V^{-1}$) due to the increased ion migration barrier and lower trap density.

The baseline drift performance of the devices was compared, as shown in Fig. 4(d). After 50 min of 3.5 V bias voltage, the $MAPbI_3$

devices fabricated by UA-annealing demonstrated significantly more stable baseline currents compared to those prepared by C-annealing (Fig. 3(d)). The current drift rates for the devices were calculated using the equation [30]

$$D = \left| \frac{J_t - J_0}{tE} \right| \quad (5)$$

where $J_t$ and $J_0$ are the current densities at the start and end points, respectively, $t$ is the duration, and $E$ is the electric field. The device based on $MAPbI_3$ thick film prepared using UA-annealing exhibited a dark current drift rate of 4.13 $nA{\cdot}cm^{-1}{\cdot}s^{-1}{\cdot}V^{-1}$, approximately four times lower than the 71.81 $nA{\cdot}cm^{-1}{\cdot}s^{-1}{\cdot}V^{-1}$ observed in that prepared by C-annealing. The higher dark current drift is attributed to the significant ion migration caused by the uneven distribution of elements.

To evaluate film uniformity, dark current measurements were

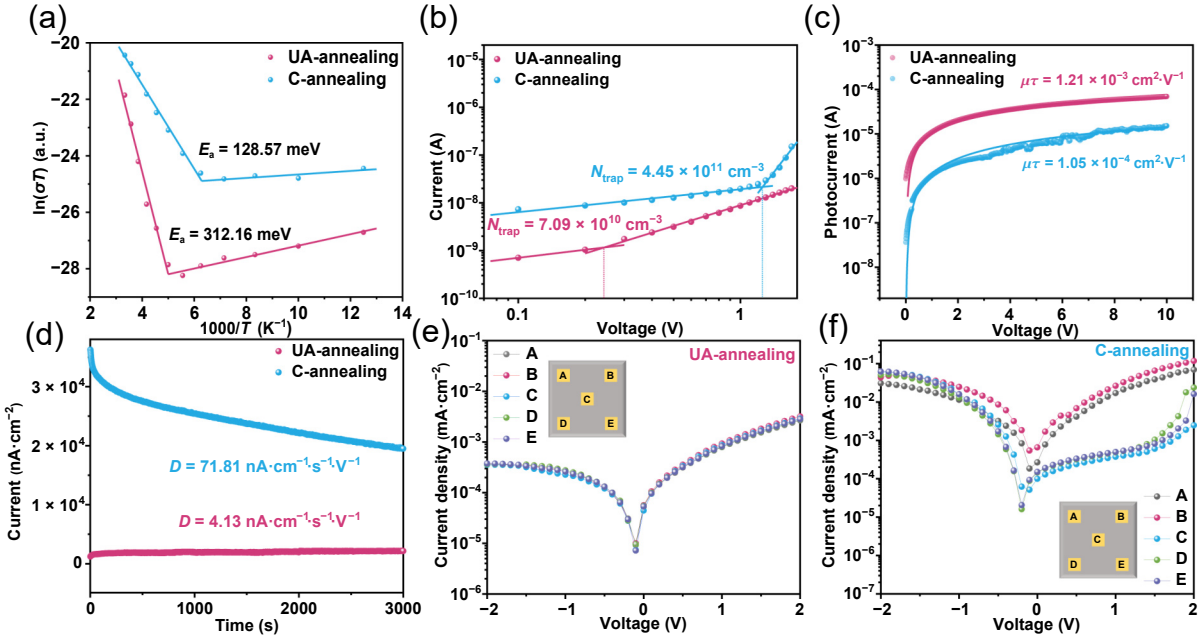


**Figure 3** (a) Temperature-dependent conductivity spectra of $MAPbI_3$ films prepared via UA-annealing and C-annealing. (b) Photoconductivity under varying bias conditions, fitted using the Hecht equation. (c) Current–voltage ($I$–$V$) curves of $MAPbI_3$ thick films. (d) Dark current drift curves of $MAPbI_3$ films. $I$–$V$ curves under dark conditions were measured at five different locations on $MAPbI_3$ thick films prepared using (e) UA-annealing and (f) C-annealing.

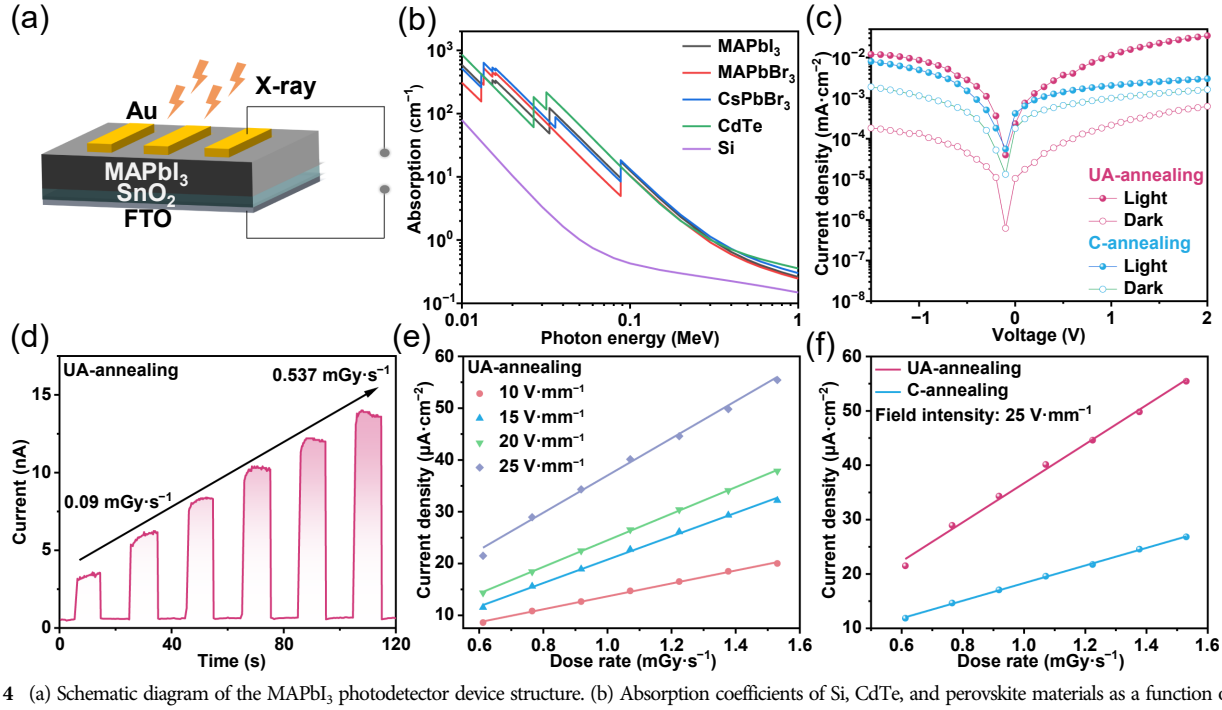


**Figure 4** (a) Schematic diagram of the $MAPbI_3$ photodetector device structure. (b) Absorption coefficients of Si, CdTe, and perovskite materials as a function of X-ray photon energy. (c) $J$–$V$ curves of $MAPbI_3$ devices prepared via two annealing methods under dark and illuminated conditions. (d) X-ray response of $MAPbI_3$ devices prepared via UA-annealing at different dose rates. (e) Sensitivity of $MAPbI_3$ photodetectors prepared using UA-annealing under various applied electric fields. (f) Comparison of sensitivity for devices prepared using the two annealing methods at a low electric field of 25 $V{\cdot}mm^{-1}$.

performed at multiple randomly selected electrode locations across each device (Figs. 3(e) and 3(f)). The UA-annealing film exhibited a two-order-of-magnitude increase in resistivity along with more stable and uniform current–voltage characteristics compared to the C-annealing processed sample. Statistical analysis of the lateral dark current uniformity further confirmed a significantly lower deviation of 6.6% for the UA-annealing film (Fig. S8 in the ESM), which is substantially smaller than that of the C-annealing counterpart (41.43%). These enhancements are consistent with the observed larger and more uniform grain sizes in the UA-annealing film, as previously illustrated. Moreover, PL mapping conducted at five distinct locations on the thick-film surfaces (Fig. S9 in the ESM) revealed highly consistent peak positions and intensities for the UA-annealing sample, indicating excellent surface homogeneity. The improved uniformity—both along the cross-section and across the surface—contributes to stable and superior electrical properties of the thick-film devices, which are essential for high-performance X-ray detection applications.

To evaluate the X-ray detection properties of the $MAPbI_3$ films, a vertical-structural (Au/$MAPbI_3$/$SnO_2$/FTO) photodetector was fabricated (Fig. 4(a)). An electron transport layer and a conductive metal layer were deposited as the cathode via thermal evaporation. Figure 4(b) shows the calculated attenuation coefficients of several typical semiconductors for different X-ray energies. $MAPbI_3$ exhibited higher attenuation coefficients than $CsPbBr_3$ and Si across the medical X-ray energy range (30–100 keV), which is attributed to the presence of heavier Pb and I atoms (Fig. S10 in the ESM). Current density–voltage curves were measured under dark and X-ray illumination conditions (Fig. 4(c)). The UA-annealing film exhibited higher photocurrents and lower dark currents compared to the C-annealing film, resulting in a higher photo-to-dark current ratio. The X-ray response was measured at different X-ray dose rates by adjusting the X-ray tube current (Fig. 4(d)). Stable dark current during testing indicated negligible ion migration. The X-ray response of the UA-annealing film was also measured at different bias voltages. At a low electric field strength of 25 V·mm$^{-1}$, the UA-annealing film exhibited a sensitivity of $3.59 \times 10^4$ μC·$Gy_{air}^{-1}$·cm$^{-2}$, much higher than the $1.62 \times 10^4$ μC·$Gy_{air}^{-1}$·cm$^{-2}$ observed for the C-annealing film (Figs. 4(e) and 4(f)).

To systematically evaluate the imaging performance of the X-ray detector fabricated using the UA-annealing process, this study employed a high-precision single-pixel scanning imaging system for quantitative characterization. As shown in Fig. 5(a), the experimental setup positioned the sample to be imaged between the X-ray source and the detector, with continuous scanning in the focal plane achieved through a precision-controlled *X*-*Y* two-dimensional translation stage. At an ultra-low dose rate of 3.2 μ$Gy_{air}$·s$^{-1}$, the detector could still clearly resolve fine structures in the metal mask target (Fig. 5(b)). To quantify the X-ray attenuation characteristics of the detector, a tunable attenuation system was constructed using multiple layers of ITO glass (the numbers in the figure indicate the glass layers). Experimental data showed that as the attenuation layer thickness increased, the response current of the UA-annealed detector exhibited a typical exponential decay pattern (Fig. 5(c)). By fitting the exponential decay model using nonlinear least squares regression, the attenuation coefficient was calculated to be 2.33 cm$^{-1}$, showing excellent agreement with the theoretically predicted value (≈ 2.4 cm$^{-1}$), thereby verifying the reliability of the measurement system.

For spatial resolution characterization, the internationally recognized slanted-edge method was employed to measure the modulation transfer function (MTF). Specifically, a single-pixel detector was used to perform point-by-point scanning of the sharp edge of a standard line pair card, with edge response data acquired by controlling sample movement along the *y*-axis via a precision displacement stage. The recorded edge spread function (ESF) was numerically differentiated to obtain the line spread function (LSF) (Fig. S11 in the ESM), from which the system's MTF curve was

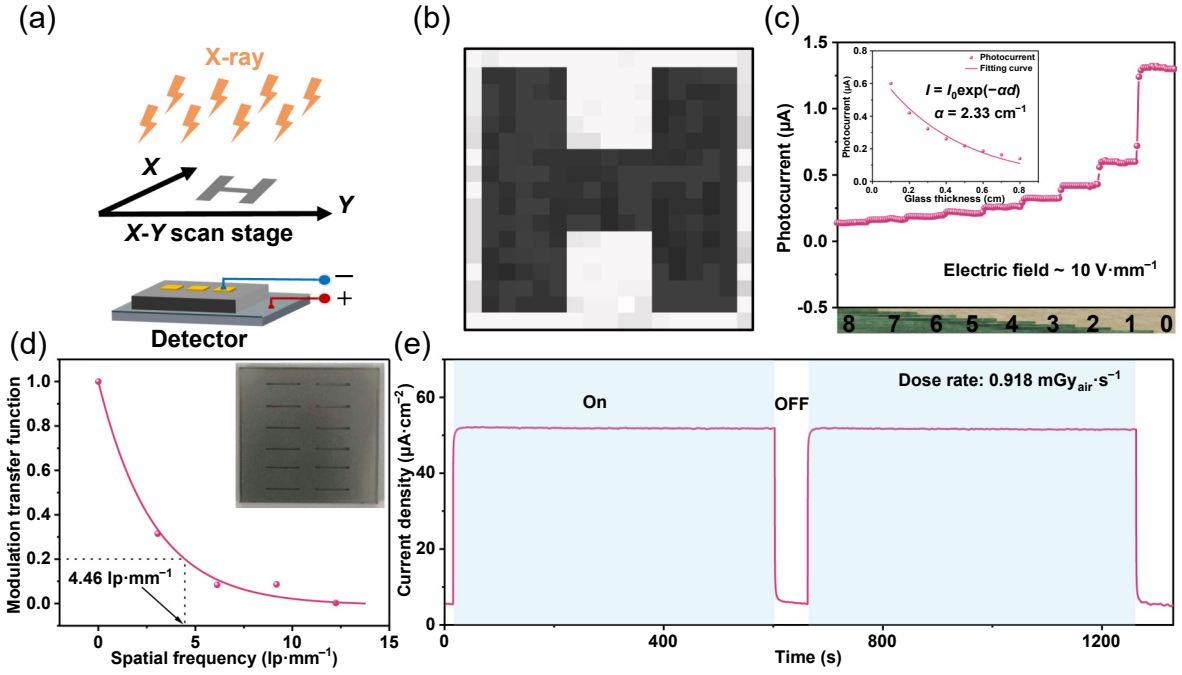


**Figure 5** (a) Schematic illustration of the setup for the X-ray imaging test. (b) X-ray imaging of a metal mask. (c) The response of the detector based on the UA-annealing film toward stacked glass coverslips. (d) MTF of the detector (the inset is the line pair card for edge spread function measurement). (e) X-ray irradiation stability of $MAPbI_3$ photodetectors prepared via UA-annealing.

derived through fast Fourier transformation (detailed calculation procedure see Note S6 in the ESM) [31]. Results demonstrated that when the MTF value decreased to 20%, the corresponding spatial resolution reached 4.46 lp·mm$^{-1}$ (Fig. 5(d)) [32, 33], significantly surpassing the performance metrics of a conventional α-Se detector. Furthermore, the long-term stability of the film under continuous X-ray irradiation was investigated (Fig. 5(e)). During a 1300-second continuous irradiation experiment at a fixed dose rate of 0.918 mGy$_{air}$·s$^{-1}$, the UA-annealed film exhibited remarkable stability with a negligible photocurrent decay rate. This excellent fatigue resistance is primarily attributed to the UA-annealing process, which effectively improves the crystalline integrity of the material and significantly reduces defect state density, thereby enhancing device durability in high-irradiation environments [34, 35]. These findings provide evidence supporting the effectiveness of the UA-annealing strategy in fabricating X-ray detectors with both outstanding uniformity and operational stability.

## 3 Conclusions

In summary, we have demonstrated that a UA-annealing process can effectively address the challenges of irregular solute ion migration and uneven distribution during the solvent volatilization of GVL-based $MAPbI_3$ precursor solutions. This method enables the fabrication of perovskite thick films with exceptional morphological smoothness and outstanding compositional homogeneity in both the horizontal and vertical dimensions. Quantitative assessments confirm a 21.5% improvement in the longitudinal homogeneity of $Pb^{2+}$ distribution over a 45 μm depth. The lateral dark current uniformity was significantly enhanced, achieving a remarkable CV of 6.6%—far superior to the 41.43% observed in C-annealing films. The superior structural uniformity directly contributes to the excellent performance of the resulting thick-film detector, which exhibits a high sensitivity of 35,900 μC·Gy$_{air}^{-1}$·cm$^{-2}$ and a high spatial resolution of 4.46 lp·mm$^{-1}$. This work thus presents a viable and novel strategy for producing high-performance, environmentally friendly, and operationally stable perovskite thick films, highlighting their strong potential for application in advanced radiation detection.

## 4 Materials and methods

### 4.1 Materials

Lead(II) iodide ($PbI_2$, 99.999%) and methylammonium iodide (MAI, 99.5%) were purchased from Advanced Election Technology Co., Ltd. γ-valerolactone (98%) was purchased from Aladdin Chemical Co., Ltd. All the chemicals were used as received without any further purification.

### 4.2 Preparation of the $MAPbI_3$ polycrystalline thick films

The FTO glass substrates were sequentially cleaned by ultrasonic treatment in soapy water, deionized water, and alcohol, followed by exposure to ultraviolet-ozone (UVO) for 15 min. $MAPbI_3$ perovskite thick films were fabricated via the blade-coating method. Initially, 0.9 mmol (0.1431 g) of MAI and 0.9 mmol (0.4149 g) of $PbI_2$ were dissolved in 200 μL of GVL. The mixture was stirred thoroughly for 6 h in a glovebox under a $N_2$ atmosphere until a homogeneous 4.5 M $MAPbI_3$ perovskite precursor slurry was obtained. The slurry was then uniformly coated onto an FTO substrate using a doctor blade, yielding a wet film. The film thickness was controlled by adjusting the gap between the blade and the substrate. Subsequently, the wet film was annealed at 60 °C in air under 40 kHz ultrasonic irradiation for 1 h, followed by a multi-stage thermal annealing process at 60 °C (2 h), 80 °C (2 h), and 100 °C (3 h). After natural cooling, a thick $MAPbI_3$ perovskite film was obtained. A control sample was prepared using the same procedure without ultrasonic treatment.

### 4.3 Device fabrication

The surface was blown with $N_2$ gas to remove any dust. Au electrodes, with a thickness of 45 μm and an area of 0.025 cm$^2$, were deposited onto the thick film surface by thermal evaporation through a pre-designed template.

### 4.4 Characterization

The XRD patterns were characterized using an X-ray diffractometer (Bruker D8 Discover). The SEM images were examined via a field-emission scanning electron microscope (JSM-IT800). The absorption spectra were recorded using a UV–vis-near infrared ray (NIR) spectrophotometer (PerkinElmer Lambda 750S) in reflection mode. The PL spectra (Ocean Insight) were used to analyze the perovskite films, while the excitation wavelength of the PL test was 415 nm. Time-resolved PL (TRPL) decay measurements were undertaken by using a Delta Flex Flux Fluorescence Lifetime System (HORIBA Scientific Company, Japan) equipped with a 485 nm pulsed diode-laser as the excitation source. The *J*–*V* characteristics of devices were recorded using a Keithley 6571B source meter. For optical response in $\mu\tau$ measurement, a monochromatic LED (365 nm light, Thorlabs M530L3) modulated by a function generator (Agilent 33210A) was used as the illumination source.

### 4.5 Detector performance measurement

The X-ray detection performance was measured on a homemade measurement system housed in the dark chamber to eliminate the impact of ambient light sources. A metal-ceramic X-ray tube (Moxtek MAGPRO 70 kV 12 W) was used as the X-ray source. X-ray photons were generated under the acceleration voltage of 50 kV with the operational current tuned from 5 to 140 μA. The *I*–*V* curves were measured with a voltage sweep rate of 0.1 V·s$^{-1}$. The dark current drift was recorded with a sampling interval of 0.01 s. The distance between the X-ray tube and the detector was tuned from 10 to 80 cm. 1 mm-thick Al plates were used as attenuators to adjust the radiation dose rate. An electrometer (Keithley 6571B) was used to apply bias voltage on the $MAPbI_3$ device and collect the response current. The X-ray dose rate was calibrated with an ion chamber dosimeter (MagicMax from IBA DOSIMETRY). MTF was achieved using the MAPbI3 film detector in linear stage-driven *X*-*Y* scanning mode.

**Electronic Supplementary Material**: Supplementary material (experimental details and additional data) is available in the online version of this article at https://doi.org/10.26599/NR.2026.94908380.

## Data availability

All data needed to support the conclusions in the paper are presented in the manuscript and the Electronic Supplementary

Material. Additional data related to this paper may be requested from the corresponding author upon request.

## Acknowledgements

This work was financially supported by National Key Research and Development Program of China (Nos. 2024YFF0507800 and 2024YFE0217100), the National Natural Science Foundation of China (Nos. U2330115, 62275206, and 22279099), Knowledge Innovation Program of Wuhan-Shuguang Project, Shenzhen Science and Technology Program (Nos. SGDX20230116093205009 and KJZD20240903101307010), Shenzhen Science and Technology Program (No. JCYJ20250604191008011), Innovation Project of OpticsValley Laboratory (No. OVL2025YZ001), and Fund for the Natural Science Foundation of Hubei Province (No. 2024AFB381).

## Declaration of competing interest

The authors declare no competing interests.

## Author contribution statement

S. K. and Z. Q. C. performed the experiments. S. K. conducted the data processing. S. K. and M. L. X. prepared the manuscript. Z. Q. C. evaluated the electronic properties of the materials. G. L. H. performed the calculations. M. L. X. directed film fabrication. S. K., Z. Q. C., M. Q. L., and X. H. performed the imaging experiments. X. H. conceived the manuscript. G. L. H., M. Q. L., and G. Y. Z. ordered the primary materials. Y. S. X., T. L. B., G. Q. L., M. L. X., and G. D. N. provided experimental conditions and funding support. All authors participated in the data analysis and contributed to the writing of the manuscript.

## Use of AI statement

None.

## References

[1] Lei, T.; Sewchand, W. Statistical approach to X-ray CT imaging and its applications in image analysis. II. A new stochastic model-based image segmentation technique for X-ray CT image. *IEEE Trans. Med. Imaging* **1992**, *11*, 62–69.

[2] Liu, Y. C.; Zhang, Y. X.; Yang, Z.; Ye, H. C.; Feng, J. S.; Xu, Z.; Zhang, X.; Munir, R.; Liu, J.; Zuo, P. et al. Multi-inch single-crystalline perovskite membrane for high-detectivity flexible photosensors. *Nat. Commun.* **2018**, *9*, 5302.

[3] Zhang, Y. X.; Liu, Y. C.; Xu, Z.; Ye, H. C.; Yang, Z.; You, J. X.; Liu, M.; He, Y. H.; Kanatzidis, M. G.; Liu, S. Nucleation-controlled growth of superior lead-free perovskite $Cs_3Bi_2I_9$ single-crystals for high-performance X-ray detection. *Nat. Commun.* **2020**, *11*, 2304.

[4] He, Y. H.; Hadar, I.; Kanatzidis, M. G. Detecting ionizing radiation using halide perovskite semiconductors processed through solution and alternative methods. *Nat. Photonics* **2022**, *16*, 14–26.

[5] Xia, M. L.; Yuan, J. H.; Niu, G. D.; Du, X. Y.; Yin, L. X.; Pan, W. C.; Luo, J. J.; Li, Z. G.; Zhao, H. T.; Xue, K. H. et al. Unveiling the structural descriptor of $A_3B_2X_9$ perovskite derivatives toward X-ray detectors with low detection limit and high stability. *Adv. Funct. Mater.* **2020**, *30*, 1910648.

[6] Ran, P.; Yang, L. R.; Jiang, T. M.; Xu, X. H.; Hui, J.; Su, Y. R.; Kuang, C. F.; Liu, X.; Yang, Y. M. Multispectral large-panel X-ray imaging enabled by stacked metal halide scintillators. *Adv. Mater.* **2022**, *34*, 2205458.

[7] Rao, H. S.; Li, W. G.; Chen, B. X.; Kuang, D. B.; Su, C. Y. *In situ* growth of 120 $cm^2$ $CH_3NH_3PbBr_3$ perovskite crystal film on FTO glass for narrowband-photodetectors. *Adv. Mater.* **2017**, *29*, 1602639.

[8] Jiang, X. M.; Fu, X. W.; Ju, D. X.; Yang, S.; Chen, Z. L.; Tao, X. T. Designing large-area single-crystal perovskite solar cells. *ACS Energy Lett.* **2020**, *5*, 1797–1803.

[9] Wei, H. T.; Fang, Y. J.; Mulligan, P.; Chuirazzi, W.; Fang, H. H.; Wang, C. C.; Ecker, B. R.; Gao, Y. L.; Loi, M. A.; Cao, L. et al. Sensitive X-ray detectors made of methylammonium lead tribromide perovskite single crystals. *Nat. Photonics* **2016**, *10*, 333–339.

[10] Rezaee, E.; Zhang, W.; Silva, S. R. P. Solvent engineering as a vehicle for high quality thin films of perovskites and their device fabrication. *Small* **2021**, *17*, 2008145.

[11] Jiao, J. M.; Yang, C. G.; Wang, Z.; Yan, C.; Fang, C. Q. Solvent engineering for the formation of high-quality perovskite films: A review. *Results Eng.* **2023**, *18*, 101158.

[12] Wu, W. Q.; Lu, H.; Han, X.; Wang, C. F.; Xu, Z. S.; Han, S. T.; Pan, C. F. Recent progress on wavelength-selective perovskite photodetectors for image sensing. *Small Methods* **2023**, *7*, 2201499.

[13] Bell, J.; Collins, R. Gamma-butyrolactone (GBL) dependence and withdrawal. *Addiction* **2011**, *106*, 442–447.

[14] Miao, Y. F.; Ren, M.; Chen, Y. T.; Wang, H. F.; Chen, H. R.; Liu, X. M.; Wang, T. F.; Zhao, Y. X. Green solvent enabled scalable processing of perovskite solar cells with high efficiency. *Nat. Sustain.* **2023**, *6*, 1465–1473.

[15] Tang, X.; Zeng, X. H.; Li, Z.; Hu, L.; Sun, Y.; Liu, S. J.; Lei, T. Z.; Lin, L. Production of γ-valerolactone from lignocellulosic biomass for sustainable fuels and chemicals supply. *Renew. Sustain. Energy Rev.* **2014**, *40*, 608–620.

[16] Li, B.; Dai, Q. L.; Yun, S. N.; Tian, J. J. Insights into iodoplumbate complex evolution of precursor solutions for perovskite solar cells: From aging to degradation. *J. Mater. Chem. A* **2021**, *9*, 6732–6748.

[17] Wang, K. X.; Liu, H.; Huang, Q.; Duan, Z. T.; Wang, J.; Zhao, C. X.; Lian, X. X.; Liu, R. C.; Su, Y.; Guan, X. et al. Controllable iodoplumbate-coordination of hybrid lead iodide perovskites via additive engineering for high-performance solar cells. *ACS Appl. Mater. Interfaces* **2024**, *16*, 50972–50981.

[18] Yalcinkaya, Y.; Hermes, I. M.; Seewald, T.; Amann-Winkel, K.; Veith, L.; Schmidt-Mende, L.; Weber, S. A. Chemical strain engineering of $MAPbI_3$ perovskite films. *Adv. Energy Mater.* **2022**, *12*, 2202442.

[19] Radicchi, E.; Mosconi, E.; Elisei, F.; Nunzi, F.; De Angelis, F. Understanding the solution chemistry of lead halide perovskites precursors. *ACS Appl. Energy Mater.* **2019**, *2*, 3400–3409.

[20] Li, Z. Z.; Zhou, F. G.; Yao, H. H.; Ci, Z.; Yang, Z.; Jin, Z. W. Halide perovskites for high-performance X-ray detector. *Mater. Today* **2021**, *48*, 155–175.

[21] Li, W. G.; Wang, X. D.; Huang, Y. H.; Kuang, D. B. Ultrasound-assisted crystallization enables large-area perovskite quasi-monocrystalline film for high-sensitive X-ray detection and imaging. *Adv. Mater.* **2023**, *35*, 2210878.

[22] Yu, D. J.; Yin, C. Y.; Cao, F.; Zhu, Y.; Ji, J. P.; Cai, B.; Liu, X. H.; Wang, X. Y.; Zeng, H. B. Enhancing optoelectronic properties of low-dimensional halide perovskite via ultrasonic-assisted template refinement. *ACS Appl. Mater. Interfaces* **2017**, *9*, 39602–39609.

[23] Xie, Z. S.; Shi, W. D.; Zheng, Y.; Tan, L. W.; Tian, Q.; Cao, Y. P.; Zhou, J. L.; Ge, X. F. Simulation investigation on impact damage characteristics of metal plate by cavitating bubble micro-jet water hammer. *Eng. Fail. Anal.* **2020**, *115*, 104626.

[24] Ye, L. Z.; Zhu, X. J.; He, Y. Micro-cutting force model of micro-jet induced by cavitation collapse in the ultrasonic field at micro-nano scale. *Int. J. Adv. Manuf. Technol.* **2022**, *119*, 3695–3702.

[25] Song, Z. H.; Du, X. Y.; He, X.; Wang, H. Q.; Liu, Z. Q.; Wu, H. D.;

Luo, H. D.; Jin, L. B.; Xu, L.; Zheng, Z. P. et al. Rheological engineering of perovskite suspension toward high-resolution X-ray flat-panel detector. *Nat. Commun.* **2023**, *14*, 6865.

[26] Ahn, S. M.; Jung, E. D.; Kim, S. H.; Kim, H.; Lee, S.; Song, M. H.; Kim, J. Y. Nanomechanical approach for flexibility of organic-inorganic hybrid perovskite solar cells. *Nano Lett.* **2019**, *19*, 3707–3715.

[27] Liu, Y. C.; Zhang, Y. X.; Zhu, X. J.; Feng, J. S.; Spanopoulos, I.; Ke, W. J.; He, Y. H.; Ren, X. D.; Yang, Z.; Xiao, F. W. et al. Triple-cation and mixed-halide perovskite single crystal for high-performance X-ray imaging. *Adv. Mater.* **2021**, *33*, 2006010.

[28] Li, N.; Feng, A. B.; Guo, X. B.; Wu, J. M.; Xie, S. D.; Lin, Q. L.; Jiang, X. M.; Liu, Y.; Chen, Z. L.; Tao, X. T. Engineering the hole extraction interface enables single-crystal $MAPbI_3$ perovskite solar cells with efficiency exceeding 22% and superior indoor response. *Adv. Energy Mater.* **2022**, *12*, 2103241.

[29] Zhang, H. J.; Wang, F. B.; Lu, Y. F.; Sun, Q. H.; Xu, Y. D.; Zhang, B. B.; Jie, W. Q.; Kanatzidis, M. G. High-sensitivity X-ray detectors based on solution-grown caesium lead bromide single crystals. *J. Mater. Chem. C* **2020**, *8*, 1248–1256.

[30] Li, N.; Li, Y. Y.; Xie, S. D.; Wu, J. M.; Liu, N. Q.; Yu, Y.; Lin, Q. L.; Liu, Y.; Yang, S.; Lian, G. et al. High-performance and self-powered X-ray detectors made of smooth perovskite microcrystalline films with 100 μm grains. *Angew. Chem.* **2023**, *135*, e202302435.

[31] Pan, W. C.; Wu, H. D.; Luo, J. J.; Deng, Z. Z.; Ge, C.; Chen, C.; Jiang, X. W.; Yin, W. J.; Niu, G. D.; Zhu, L. J. et al. $Cs_2AgBiBr_6$ single-crystal X-ray detectors with a low detection limit. *Nat. Photonics* **2017**, *11*, 726–732.

[32] Xie, G. S.; Li, H.; Qiu, L. B. Recent advances on monolithic perovskite-organic tandem solar cells. *Interdiscip. Mater.* **2024**, *3*, 113–132.

[33] Yi, Z. J.; Li, X.; Xiong, Y. C.; Shen, G. B.; Zhang, W. G.; Huang, Y. H.; Jiang, Q. H.; Ng, X. R.; Luo, Y. B.; Zheng, J. H. et al. Self-assembled monolayers (SAMs) in inverted perovskite solar cells and their tandem photovoltaics application. *Interdiscip. Mater.* **2024**, *3*, 203–244.

[34] Sun, L.; Li, W.; Zhu, W.; Chen, Z. L. Single-crystal perovskite detectors: Development and perspectives. *J. Mater. Chem. C* **2020**, *8*, 11664–11674.

[35] Feng, A. B.; Jiang, X. M.; Zhang, X. Y.; Zheng, X. P.; Zheng, W. T.; Mohammed, O. F.; Chen, Z. L.; Bakr, O. M. Shape control of metal halide perovskite single crystals: From bulk to nanoscale. *Chem. Mater.* **2020**, *32*, 7602–7617.